Journal of Renewable and Sustainable Energy ARTICLE scitation.org/journal/rse

Can lidars assess wind plant blockage in simple terrain? A WRF-LES study

Cite as: J. Renewable Sustainable Energy **14**, 063303 (2022); doi: 10.1063/5.0103668
Submitted: 16 June 2022 · Accepted: 30 September 2022 ·
Published Online: 8 November 2022

View Online Export Citation CrossMark

Miguel Sanchez Gomez,[1,a)] Julie K. Lundquist,[1,2] Jeffrey D. Mirocha,[3] Robert S. Arthur,[3] Domingo Muñoz-Esparza,[4] and Rachel Robey[5]

AFFILIATIONS

[1]Department of Atmospheric and Oceanic Sciences, University of Colorado Boulder, Boulder, Colorado 80309, USA
[2]National Renewable Energy Laboratory, Golden, Colorado 80401, USA
[3]Lawrence Livermore National Laboratory, Livermore, California 94550, USA
[4]National Center for Atmospheric Research, Boulder, Colorado 80305, USA
[5]Department of Applied Mathematics, University of Colorado Boulder, Boulder, Colorado 80309, USA

Note: This article is part of the special issue Preparatory Work for the American Wake Experiment (AWAKEN).
[a)]**Author to whom correspondence should be addressed:** misa5952@colorado.edu

ABSTRACT

Wind plant blockage reduces wind velocity upstream of wind plants, reducing the power generated by turbines adjacent to the inflow, and potentially throughout the plant as well. The nature of the mechanism that amplifies blockage as well as the velocity reductions in both the induction zone and potentially deeper into the array are not well understood. Field observations can provide valuable insight into the characteristics of the induction zone and the mechanisms that amplify it. However, the relatively small velocity reductions that have been measured experimentally pose a challenge in quantifying blockage, especially in onshore environments with flow heterogeneities that may be of the same scale as the blockage effect itself. We simulate the flow around the King Plains wind plant in the relatively simple terrain of Oklahoma, the location of the American WAKE experimeNt, to evaluate wind plant blockage in this environment. Using numerical simulations, we find the largest velocity deceleration (0.64 m s^{-1}; 8%) immediately upstream of the wind plant, and 1% velocity deficits 24 rotor diameters upstream of the first turbine row. We also use virtual measurements upstream of the wind plant to analyze the uncertainties and difficulties in measuring blockage using a scanning lidar on shore. Based on our virtual lidar study, the induction zone of land-based wind plants can be incorrectly estimated using observations if the effects of nonuniform terrain on the flow are not carefully considered. Changes in terrain elevation produce local variations in wind speed (as measured by a scanning lidar) that exceed in magnitude the deceleration within the induction zone. We refer to these local changes in wind speed as terrain effects. A methodology to differentiate between terrain effects and blockage in experimental settings is proposed and evaluated herein, highlighting the difficulties and uncertainties associated with measurement and simulation of blockage in even relatively simple onshore environments.

I. INTRODUCTION

Wind turbines extract kinetic energy from the wind, thereby reducing its velocity downstream. As a result, turbines downstream experience slower wind speeds with more turbulence and produce less power, an effect known as wake loss. Wind speed also decreases upstream of turbines as they obstruct the flow. This blockage effect occurs over a region called the induction zone. For single turbines, the induction zone is caused by a pressure stagnation, resulting in a pressure gradient force oriented opposite to the inflow direction that reduces the flow speed approaching the turbine. The induction region of wind plants forms from the superposition of the induction of the individual turbines in the array and may be further amplified by a larger-scale interaction between the boundary layer and the turbine array.[1–7] In this way, we consider blockage as the velocity deceleration upstream of a wind plant relative to freestream conditions. Generally, wake effects are accounted for in power forecasting methods that employ deterministic tools.[3,8,9] However, wind plant blockage is usually neglected,

possibly resulting in lower-than-forecasted energy predictions and financial losses for wind plant operators.[10]

Whereas wind speed deficits from wakes are large (∼10%),[11] wind plant blockage produces wind speed deficits of ∼1%,[3,12–14] making it much more difficult to quantify, especially in experimental setups. Experimental results and high-fidelity numerical simulations show wind speed slowdowns between 1% and 5% of freestream at 1.5–3 rotor diameters (1.5D–3D) upstream of wind plants.[3,7,13] Simplified models, such as linearized models[2,15] and analytical vortex models,[16] comparably report velocity deficits between 2% and 3% at 2.5D upstream of wind plants. Some simplified models, however, do not include important physical mechanisms that likely amplify blockage, such as atmospheric stability and wind speed shear.[17] A limited number of simulations suggest wind decelerations larger than 10% at a distance of 2D upstream of the first row of turbines.[4,7] Wu and Porté-Agel[7] found large deficits (10% deficit 2.5D upstream) in their strong free-atmosphere stratification case that coincide with gravity wave formation, whereas gravity waves did not form in their weak free-atmosphere stratification case and the deficits from blockage remained small (1.2% deficit 2.5D upstream). Note that for 10 m s^{-1} hub-height winds, the blockage effect is of the same order of magnitude as the precision of state-of-the-art remote sensing instruments, such as scanning lidars (∼0.1 m s^{-1}).

Another challenge in quantifying blockage is that the induction zone covers a large area upstream of the wind plant, the extent of which can change. Both numerical and experimental studies show the extent and magnitude of the induction zone can vary substantially depending on the size and layout of the wind plant, atmospheric conditions, wind turbine characteristics, and wind speed.[3–5,7,12,18] Although some studies show detectable decelerations up to 30D upstream,[3,7,12,18] others suggest decelerations that extend up to ∼80D upstream of the first row of the wind plant.[4,7] The large spread in the results primarily comes from gravity waves forming and amplifying blockage in idealized simulations. The large and uncertain extent of the induction zone, and the small wind speed deficits detected therein, make blockage difficult to quantify, especially in field experiments.

At present, there is no established methodology for experimentally measuring wind plant blockage. Generally, studies define a freestream velocity that approximates the undisturbed flow to estimate the blockage effect. Wind tunnel experiments estimate the freestream velocity using point measurements far upstream of the wind plant.[18] Various methodologies are used to quantify blockage in operational wind plants. Schneemann *et al.*[12] quantify the magnitude of upstream blockage in an operational offshore wind plant using scanning lidar measurements. They estimate a freestream velocity for each scan using the mean wind speed across the whole sampling area, which includes the induction zone region.[12] Bleeg *et al.*,[3] Jacquet *et al.*,[13] and Sebastiani *et al.*,[14] on the other hand, employ a statistical approach to differentiate between wind speed measurements before and after the commercial operation date (COD) of several land-based wind plants, finding that these induce lower wind speeds upstream (<5% deficits). Still, the community lacks consensus on a quantitative definition for the unperturbed conditions upstream of operational wind plants (i.e., how far upstream is "unperturbed") and, hence, the blockage effect.

Topographic variations and changes in land cover pose additional difficulties in measuring the induction zone of wind plants. In ideal and homogeneous atmospheric conditions offshore, the flow upstream of a wind plant can be uniform, facilitating the detection of blockage onsite, for instance, with scanning lidars.[12] Conversely, on shore, the velocity field varies spatially due to terrain and changes in surface forcing (e.g., heterogeneous surface roughness[19] or temperature[20]). Terrain-forced flows and thermally driven circulations, for example, can produce significant (∼1 m s^{-1})[21,22] wind speed fluctuations, obscuring the slowdown caused by wind plant blockage. Previous studies were able to isolate blockage from other phenomena by employing long-term wind speed measurements before and after the COD of onshore and offshore wind plants.[3,13,14] Though this methodology implicitly accounts for spatial changes in wind speed (for example, due to terrain), it is impractical for quantifying blockage in already operational wind plants, or over short time periods, or when the surface vegetation changes over the life of the wind plant.[23]

Here, we analyze blockage for a wind plant located in relatively simple terrain and evaluate the difficulties and uncertainties of quantifying the induction zone using field-like observations. To this end, we (1) characterize the induction zone of a wind plant in central Oklahoma using simulation results, (2) quantify the blockage effect using virtual measurements, and (3) evaluate the errors associated with measuring wind plant blockage around simple but nonnegligible terrain features. The test site is the King Plains wind plant, which is located in Oklahoma and is the central location for the American WAKE experimeNt (AWAKEN) field campaign.[24]

The remainder of the paper is structured as follows: A brief description of the climatology of central Oklahoma is given in Sec. II. The simulation setup is presented in Sec. III. In Sec. IV, we introduce the criteria and the atmospheric conditions for a case study. The process of generating turbulence in nested mesoscale–microscale simulations is outlined in Sec. V. We characterize the induction zone of the wind plant in Sec. VI and present a method for quantifying the blockage effect from observations around simple terrain in Sec. VII. Finally, in Sec. VIII, we provide a summary of our findings and suggestions for future work to further improve understanding of the wind plant blockage effect.

II. CLIMATOLOGY OF CENTRAL OKLAHOMA

The U.S. Department of Energy's Atmospheric Radiation Measurement (ARM) program's Southern Great Plains (SGP) site offers long-term atmospheric instrumentation in central Oklahoma. A brief description of the climatology at this site is provided here, and a more thorough analysis can be found in Krishnamurthy *et al.*[25] and Debnath *et al.*[26]

Hub-height winds at the ARM-SGP site are predominantly southerly throughout the year (Fig. 1). From 2013 to 2019, the wind direction distribution is bimodal, with 36% southerly winds and 25% northerly.[25] Southerly flow also dominates during stable conditions.[25] The wind speed distribution at 90 m above ground level (AGL) can be characterized by a Weibull distribution with shape parameter $k = 8.49$ m s^{-1} and scale parameter $\lambda = 2.22$. Wind speed and wind direction exhibit large shear in the surface layer, especially during stable conditions.[26] The median wind speed shear exponent between 10 and 169 m is 0.09 and 0.323 for unstable and stable conditions, respectively. The median wind veer is 0.045 and 0.116 ° m^{-1} during unstable and stable conditions, respectively. Moderately stable conditions promote the formation and persistence of wakes from wind farms in the region.[28]

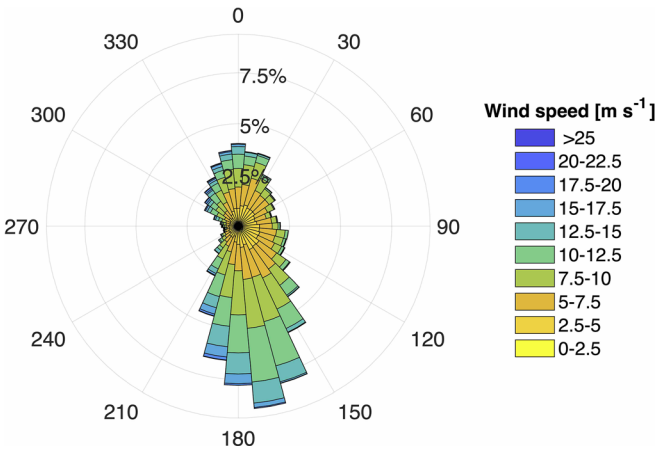

FIG. 1. Wind rose at 90 m above the surface estimated using data from a Doppler profiling lidar[27] at the ARM-SGP central facility for the year 2018.

Turbulence measurements at the ARM-SGP site show evidence of a strong diurnal cycle and seasonal variability. Convective daytime periods consistently show increased turbulence relative to stable nighttime periods. On average, turbulence kinetic energy (TKE) at the surface remains nearly constant at 0.5 $m^2\ s^{-2}$ during nighttime (02:00–12:00 UTC) and exceeds 1 $m^2\ s^{-2}$ during daytime.[25] Similarly, the vertical velocity variance above the surface layer exceeds 1 $m^2\ s^{-2}$ during peak convective conditions (20:00 UTC) and remains below 0.2 $m^2\ s^{-2}$ during nighttime conditions (see Fig. 30 in Krishnamurthy *et al.*[25]). The strong diurnal cycle is amplified during the summer months (June, July, and August).

Nocturnal low-level jets (LLJs) are consistently observed at this location.[25,26,28] Nocturnal LLJs generally persist between approximately 03:00 and 14:00 UTC (see Fig. 23 in Krishnamurthy *et al.*[25]) The jet's nose is generally below 600 m AGL. During the summer months, 40% of the LLJ occurrences display the wind speed maximum between 400 and 700 m.[25] Furthermore, most of the LLJs take place during southerly winds.[26] Increased turbulence is observed below the nose of the LLJ, caused by large vertical wind shear between the nose and the surface.

III. SIMULATION SETUP

We perform nested mesoscale–microscale simulations over central Oklahoma using the Weather Research and Forecasting (WRF) model[29] v4.1.5 with turbines modeled using a generalized actuator disk (GAD) approach. WRF is a fully compressible, nonhydrostatic model that solves the Navier–Stokes and thermodynamic equations for large Reynolds number fluids (no viscosity or thermal conductivity). WRF uses an Arakawa-C grid staggering in the horizontal and a terrain-following, hydrostatic-pressure vertical coordinate. Equations are integrated in time using a third-order Runge–Kutta scheme with a smaller time step for acoustic modes. The advection terms are spatially discretized using an even/odd-order numerical scheme.

Synoptic-scale events and turbulent eddies are concurrently represented by using a four-domain, one-way nested setup centered at the King Plains wind plant (Fig. 2). The first two domains, D01 and D02, utilize the Mellor–Yamada–Janjic planetary boundary layer parameterization[30] for turbulence closure. The third and fourth domains, D03 and D04, use the nonlinear backscatter and anisotropy model with TKE-based stress terms from Kosović,[31] implemented in WRF by Mirocha *et al.*,[32] to parameterize subgrid-scale (SGS) fluxes of momentum and heat. The physical characteristics of the domains are provided in Table I.

The innermost large-eddy simulation (LES) domain (D04) is shifted southward of the King Plains wind plant to ensure a sufficient fetch for turbulence to equilibrate with the mean flow [Fig. 2(c)]. Turbines in D04 are close to the lateral domain boundaries, possibly modifying the blockage effect of the wind plant.[17,33] However, an LES

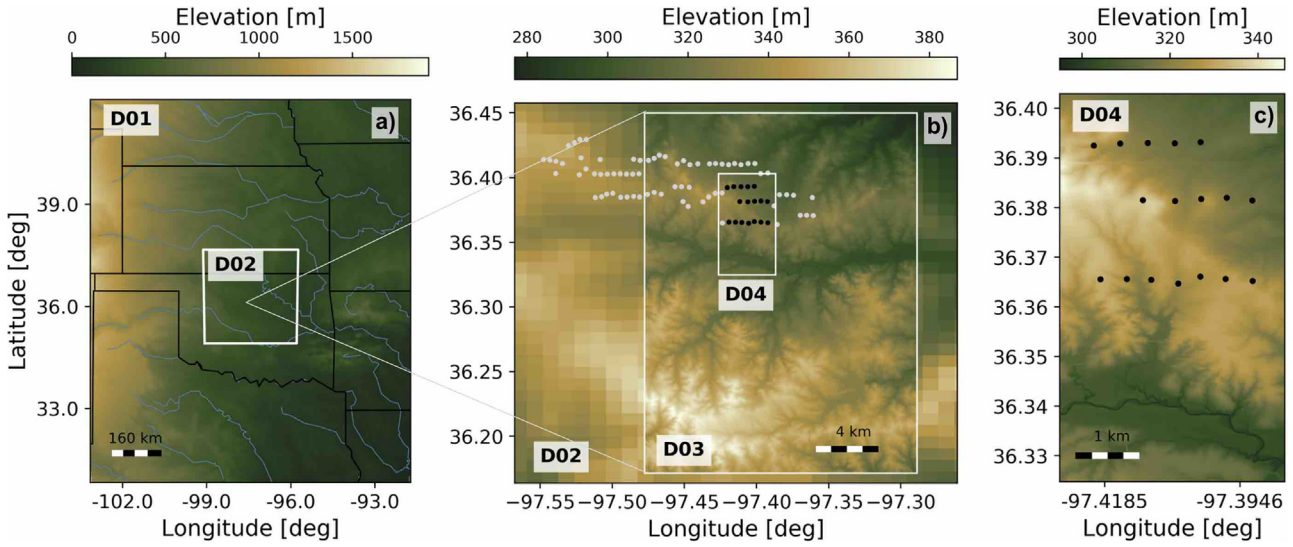

FIG. 2. Topographic map for the mesoscale (D01 and D02) and microscale (D03 and D04) domains. The black lines in (a) represent state lines, and the blue lines represent the major rivers. Turbines in the King Plains wind plant are represented by gray circles (b). Turbines simulated herein are represented by black circles (b) and (c).

TABLE I. Simulation setup, including horizontal resolution, domain size, vertical resolution at the surface, and whether or not the cell-perturbation method is activated in the domains.

Domain	Δx (m)	L_x (km)	L_y (km)	L_z (km)	Δz_s (m)	n_x, n_y, n_z	Cell perts.
D01	5000	1100	1500	16.73	8	220, 300, 79	No
D02	1000	300	300	16.73	8	300, 300, 79	No
D03	62.5	17	31	16.73	8	272, 496, 79	Yes
D04	3.9	3.6	8.7	16.73	4	913, 2225, 158	Yes

domain that is wide enough to cover the King Plains wind plant and leaves considerable space in between the edge most turbines and the lateral boundaries is not computationally feasible. Also note that D04 uses higher resolution in the vertical direction[34] to resolve turbulence structures in stable conditions. High-resolution topography (1/3 arc-second) from the 3D Elevation Program[35] and land use (1 arc-second) data from the National Land Cover Database[36] are used for domains D03 and D04 to have an appropriate turbulence forcing from the topography and land cover.

All domains use WRF Single-Moment 3-class microphysics,[37] Rapid Radiative Transfer Model longwave radiation,[38] and Dudhia shortwave radiation[39] schemes. The Eta similarity surface layer parameterization,[40] based on Monin–Obukhov similarity, is employed with the Noah Land Surface Model.[41] Boundary conditions for D01 are provided by 12 km analysis from the North American Mesoscale Forecast System.[42]

We simulate the wind turbines exclusively in the innermost domain (D04) using the generalized actuator disk implemented by Mirocha *et al.*[43] and modified by Aitken *et al.*[44] and Arthur *et al.*[45] The NREL 5 MW wind turbine has a hub height of 90 m, rotor diameter D of 126 m, cut-in speed of 3 m s^{-1}, rated speed of 11.4 m s^{-1}, and cutout speed of 25 m s^{-1}. Note that turbines at the King Plains wind plant are GE 2.82 MW wind turbines, with a hub height of 89 m and rotor diameter of 127 m. Our simulations use the NREL 5 MW turbine given that the specifications for the GE 2.82 MW are not publicly available. It is likely that the blockage effect is amplified by using a turbine with higher rated power.

IV. CASE STUDY

We use several criteria to find a case study that best displays wind plant blockage at the King Plains wind plant. Wind plant blockage has been observed in offshore environments only during stably stratified boundary layers and winds below rated speed.[12] As a result, we consider a time period with a stably stratified boundary layer and hub-height wind speeds between cut-in and rated speed. Furthermore, wind speed and wind direction should remain nearly steady to facilitate the detection of the blockage effect.

The nine-day period in 2018, June 10–18, exhibits strong and repeated occurrences of nocturnal low-level jets,[28] typical for this region. We performed mesoscale simulations of June 10–18, 2018, using domains D01 and D02 to characterize the atmospheric conditions and find a test case for evaluating wind plant blockage. From these 9 days, June 18 exhibits the best fit to our criteria for stability and wind speed.

A. June 18, 2018

The structure of the boundary layer on June 18, 2018, consists of an initially weakly convective surface layer that transitions to a stably stratified boundary layer characterized by strong shear and veer of the horizontal velocity (Fig. 3). A nocturnal low-level jet forms shortly past sunset (03:00 UTC) driven by a rapidly forming stable layer below the capping inversion ($z \approx 1500$ m). The low-level jet initially displays a deep vertical extent from 400 to 1400 m, evolving to a shallow jet with the maximum wind speed at 600 m after 05:30 UTC. The change in the structure of the nocturnal jet is likely driven by increasing static stability. Winds are consistently southerly throughout the night, with strong wind veer (~0.046° m^{-1}) below the LLJ nose, typical for this region.[25,26]

Atmospheric conditions in the surface layer remain quasi-steady before sunrise on June 18, 2018, providing ideal conditions for evaluating wind plant blockage. Hub-height wind speed and wind direction stabilize to approximately 7.5 m s^{-1} and 175° after 09:30 UTC [Figs. 4(a) and 4(b)]. Similarly, static stability, as quantified by the bulk Richardson number in the lowest 200 m of the boundary layer, remains nearly unchanged [Fig. 4(c)]. The bulk Richardson number is defined as $Ri = \frac{g\Delta\theta_v \Delta z}{T_v(\Delta u^2 + \Delta v^2)}$, where g is the gravitational acceleration, T_v is the virtual temperature of the layer of thickness Δz, $\Delta\theta_v$ are the virtual potential temperature difference across the layer, and Δu and Δv are the changes in horizontal wind components across the layer. Note that winds in the LES domains are expected to differ slightly from the mesoscale as turbulence structures start to be resolved.

Spin-up time varies for every domain. The mesoscale domains (D01 and D02) are initialized at 16:00 UTC June 17, 2018 and 22:00 UTC June 17, 2018, respectively. The first LES domain (D03) is initialized at 08:30 UTC June 18, 2018. Turbulence is fully developed in D03 after 1 h of spin-up time. The innermost LES domain (D04) then starts

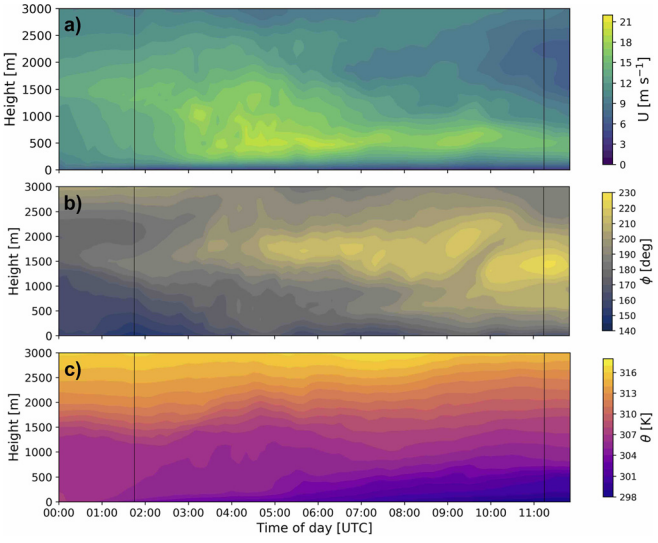

FIG. 3. Time-height horizontal wind speed (a), wind direction (b), and potential temperature (c) for D02 on June 18, 2018, at the location of the King Plains wind plant. Sunset and sunrise are illustrated for reference with the black lines at 01:45 UTC and 11:14 UTC, respectively.

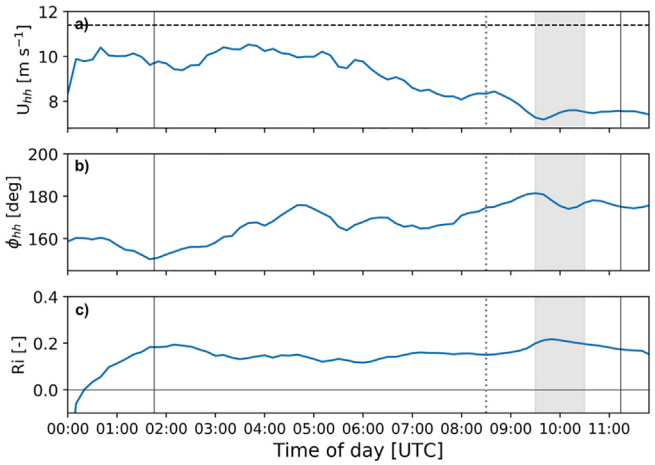

FIG. 4. Time series of hub-height wind speed (a), hub-height wind direction (b), and the bulk Richardson number (c) for D02 on June 18, 2018, at the location of the King Plains wind plant. The bulk Richardson number is estimated between 10 and 200 m. Sunset and sunrise are illustrated for reference with the solid black lines at 01:45 UTC and 11:14 UTC, respectively. The dashed black line in (a) represents rated speed for the NREL 5 MW turbine. The dotted gray lines represent initialization time for D03 and the gray shaded area represents the simulation time for D04.

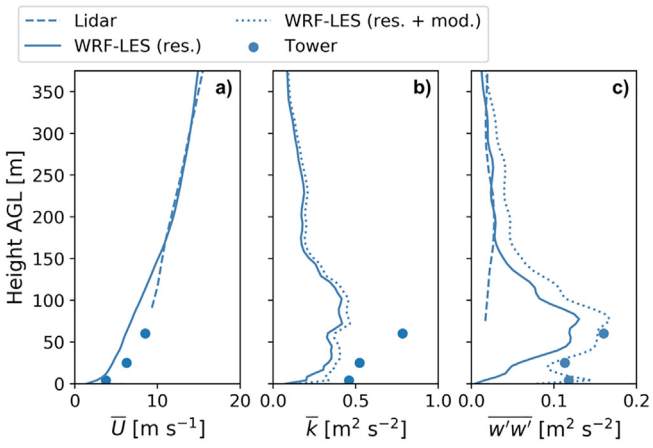

FIG. 5. Mean horizontal wind speed (a), turbulence kinetic energy (b), and vertical velocity variance (c) for simulations and observations. Mean wind speed and turbulence quantities from D04 are compared with data from the ARM-SGP site[27,46,47] from 10:00 to 11:00 UTC, June 18, 2018. The turbulence kinetic energy ($\overline{k}$) and vertical velocity variance ($\overline{w'w'}$) for the simulations are estimated using a 20-min moving variance. Data from the ARM-SGP site are temporally averaged using 30-min time windows. The dotted line in (b) and (c) represents the sum of resolved and modeled turbulence in the LES.

at 09:30 UTC June 18, 2018. We let turbulence spin up in D04 for 30 min, after which we run the simulations for another 30 min to evaluate wind plant blockage.

We validate model results using observations in the vicinity of the King Plains wind plant. The ARM-SGP site offers long-term observations for a qualitative validation. A quantitative comparison between the simulations and observations is not possible due to the distance between the two sites and the coarse temporal resolution of the ARM-SGP data. Although the ARM's SGP site is 25 km away from our innermost LES domain, it serves as an approximation for turbulence statistics and mean flow conditions within our domain due to similar terrain and vegetation characteristics.

Turbulence and mean atmospheric conditions are well represented in the LES compared to observations in this region (Fig. 5). Turbulence statistics are estimated using Reynolds decomposition, where the flow velocity (u_i) is decomposed into fluctuating (u_i') and mean ($\overline{u_i}$) components ($u_i' = u_i - \overline{u_i}$). From now on, temporal averaging is denoted by an overbar ($\bar{}$) and spatial averaging along the i-direction by angled brackets $\langle\,\rangle_i$. WRF-LES can reproduce the mean wind speed throughout the boundary layer. Horizontal wind speed from the LES matches the lidar estimates above 150 m. Below 150 m, model results slightly underestimate the horizontal wind speed measured at the ARM-SGP site. (Of course, the wind speeds at the ARM-SGP site may be influenced by turbines nearby, as shown by Bodini *et al.*[28]) Turbulence statistics are also well represented. Though turbulence kinetic energy ($\overline{k}$) is underestimated in WRF-LES, the total (resolved and modeled) vertical velocity variance ($\overline{w'w'}$) exhibits very similar characteristics to the data from the sonic anemometers at the ARM-SGP site. The variances of the horizontal velocities are underrepresented in WRF-LES, perhaps due to unresolved terrain and vegetation variability. The vertical velocity variance measured by the lidar also concurs with WRF-LES above 150 m. The lidar suggests smaller variance of the vertical velocity within the turbine rotor layer than the LES. Nonetheless, the lidar also displays much lower $\overline{w'w'}$ values compared to the sonic anemometer even though both are at the same location.

V. TURBULENCE GENERATION IN NESTED MESOSCALE-LARGE-EDDY SIMULATIONS

To reduce the fetch required to develop three-dimensional turbulence in the nested LES domains, we use the cell-perturbation method (CPM).[48,49] The CPM adds random perturbations to the potential temperature field in the outer 24 grid points of the lateral inflow domain boundaries to instigate three-dimensional turbulent motions within the boundary layer. As proposed by Muñoz-Esparza *et al.*,[49] the maximum perturbation amplitude $\tilde{\theta}_{pm}$ corresponds to a perturbation Eckert number, $Ec = U_g^2/(c_p\tilde{\theta}_{pm}) = 0.2$, where U_g is the geostrophic wind speed, and $c_p = 1005\,\mathrm{J\ kg^{-1}\ K^{-1}}$ is the specific heat capacity of air at constant pressure. Furthermore, the perturbation time step t_p correspond to a dimensionless timescale $\Gamma = t_p U_1/d_c = 1$, where U_1 is the horizontal wind speed at the first vertical grid-point imposed on the LES boundary, and d_c is the diagonal grid-cell length. The boundary layer height, z_i, is diagnosed in the boundary layer parameterization from the mesoscale domains and fed into the LES domains. For the Mellor–Yamada–Janjic scheme, z_i is defined as the height where the modeled turbulence kinetic energy decays below a certain threshold ($\overline{k} \leq 0.101\ \mathrm{m^2\ s^{-2}}$). For the simulated time period, the mean boundary layer height was within 30 m of the nose of the nocturnal low-level jet.

Turbulence in D04 propagates over the entire domain and stabilizes after 20 min of spin-up time (Figs. 6 and 7). Although turbulence stabilizes faster closer to the inflow boundary, turbulence quantities in the rest of the domain remain nearly constant in time after 09:50 UTC

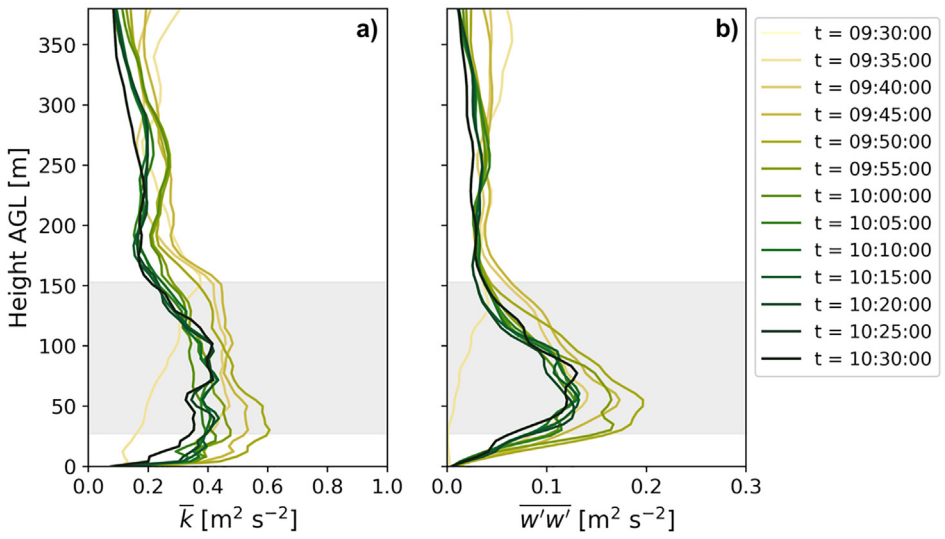

FIG. 6. Temporal evolution of turbulence kinetic energy (a) and vertical velocity variance (b) for D04 on June 18, 2018. Vertical profiles are sampled at Easting: $x = 900$ m, Northing: $y = 4492$ m in domain. The turbulence kinetic energy ($\overline{k}$) and vertical velocity variance ($\overline{w'w'}$) are estimated using a 20-min moving variance. The gray shaded region represents the turbine rotor layer.

(Fig. 6). Furthermore, turbulence propagates across all scales after 1.2 km of fetch (Fig. 7). The turbulence spectra of v and w in the turbine rotor layer approach self-similarity 1.2 km away from the southern inflow boundary. The integral length scale at hub height also remains nearly constant over the fully turbulent region of the domain $\langle l_v \rangle_{xy} = 68$ m (not shown). It is expected to have some spatial variability in turbulence caused by changes in terrain forcing. A sensitivity analysis on horizontal and vertical grid resolution proved $\Delta x = 3.9$ and $\Delta z_s = 4$ m is sufficient to consistently resolve at least 80% of the total TKE in the innermost domain for $z > 35$ m AGL (see Appendix for additional information).

VI. WIND PLANT BLOCKAGE

We first evaluate wind plant blockage using two sets of simulations, one with and one without turbines in the domain. This setup allows us to differentiate wind plant blockage from terrain-induced effects, non-stationarity, and time-evolving boundary conditions. Because the only difference between the two simulations is the inclusion of turbines with the GAD, the difference in their velocity fields can be attributed to the effect of the turbines on the flow. The LES velocity fields are temporally averaged over 30 min of simulation time. The time-averaged, hub-height velocity deficit ($\Delta\bar{U} = \bar{U}_{\mathrm{GAD}} - \bar{U}$) shows signatures of both downstream wake effects and upstream blockage (Fig. 8). Whereas wakes result in wind speed deficits larger than 4 m s^{-1}, the deficits upstream of the wind plant are less than 1 m s^{-1}. To account for spatial variability in the velocity deficit, we also perform a spatial average along the west–east direction upstream of the wind plant to extract the cumulative effect of the turbines in the flow.

We define the induction zone using the velocity deficit upstream of the first row of turbines in the plant, applying statistical significance testing. For the statistical analysis, we consider the west–east averaged velocity ($\langle \bar{U} \rangle_x$) over the region upstream of the wind plant (from $x = 535$ to $x = 3050$ m in domain). Furthermore, we subsample the velocity field from the LES grid every integral length scale ($l_v = 67.9$ m) to ensure statistical independence (spatially) between each data point. Statistical independence in the temporal domain is guaranteed by sampling the velocity field every 30 s, a longer period than the integral timescale at hub height. The two-sided 95% confidence intervals on the temporally and spatially averaged velocity fields at each distance upstream (in 0.5D increments) are estimated using a bias-corrected and accelerated bootstrapping method, resampling 10 000 times with replacement.[50]

The induction zone of the wind plant extends 24D (3024 m) upstream of the first turbine row (Fig. 9). We employ statistical significance testing to determine the extent of the induction zone. In such a way, the induction zone is bound by the farthest location upstream of the wind plant that exhibits a mean velocity deficit statistically different from zero using a 95% confidence level. The velocity field from the simulation with the GAD is only statistically different from the simulation without the GAD between $y = 1413$ and $y = 4437$ m (between −24D and 0D upstream of the southernmost turbine). South of $y = 1413$ m, the velocity deficit displays an asymptotic behavior toward zero, suggesting that the blockage effect would remain unchanged with a longer domain. However, a wider domain in the cross-stream direction might modify the blockage effect of the wind plant.[17,33] As expected, the largest flow deceleration in the induction zone takes place closest to the first turbine row ($\langle \Delta\bar{U} \rangle_x = -0.64$ m s^{-1}; $\langle \Delta\hat{\bar{U}} \rangle_x = -8\%$). Moreover, 5D upstream of the southernmost turbine, the velocity deficit is −0.319 m s^{-1} ($\langle \Delta\hat{\bar{U}} \rangle_x = -3.92\%$). Though the induction zone extends very far upstream of the wind plant, the magnitude of the velocity deficit remains below 10% of the freestream wind speed (based on the simulation without turbines) throughout.

VII. WIND PLANT BLOCKAGE ASSESSED BY A VIRTUAL SCANNING LIDAR

In Sec. VI, we isolated the effect of the turbines in the flow by running two sets of simulations, one with and one without the GAD in the domain. However, in experimental settings, it is not possible to isolate turbine effects from the mean flow. The experimental counterpart of simulations with and without the GAD would be to turn off turbines in the wind plant, which is unrealistic given the associated costs for wind plant operators. Here, we explore the difficulties in

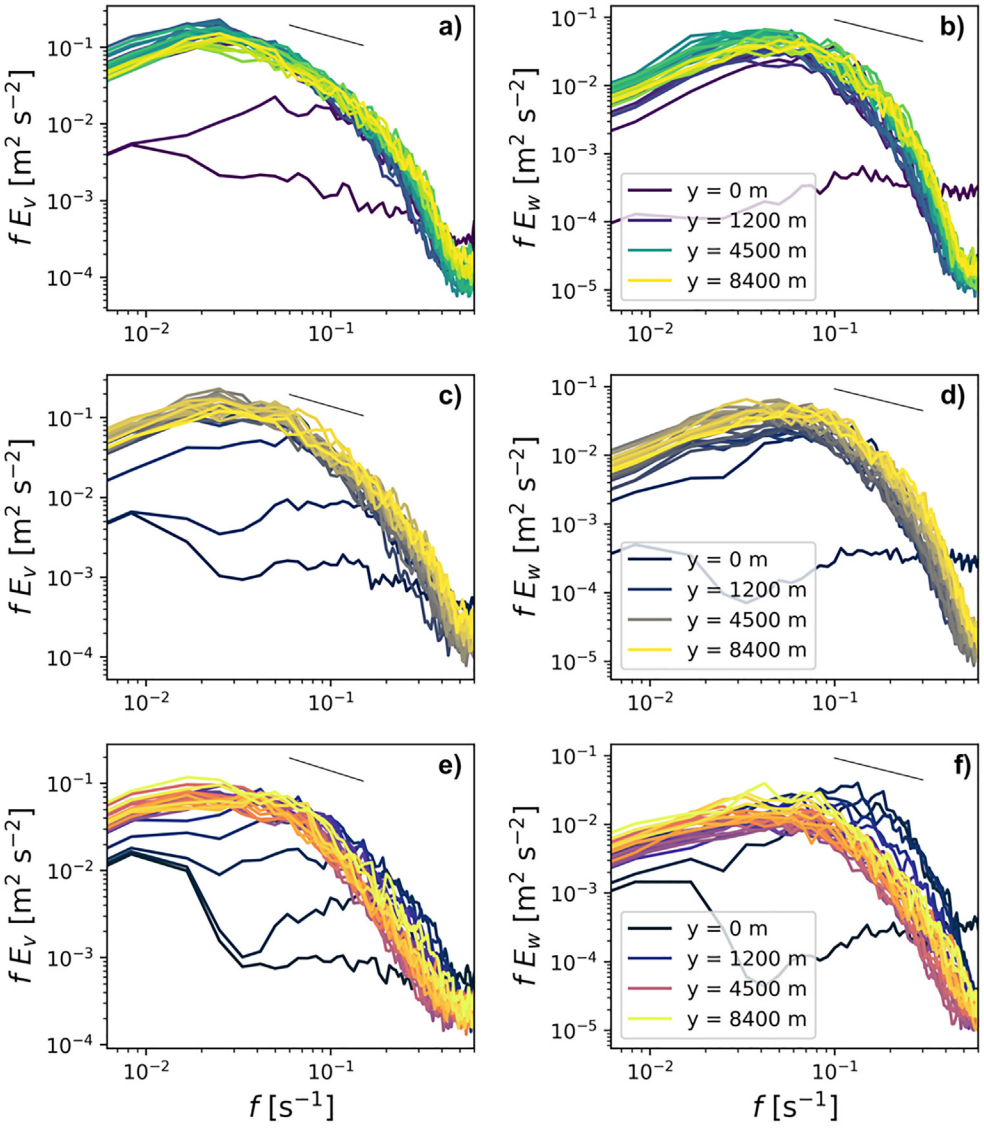

FIG. 7. Development of compensated velocity spectra for the meridional (v) and vertical (w) velocities in the streamwise direction at $z = 50$ (a) and (b), $z = 90$ (c) and (d), and $z = 150$ m (e) and (f). The theoretical $-2/3$ Kolmogorov slope for the inertial range is indicated by the solid black line in each plot. Colored lines indicate distance from the inflow southern boundary in 300 m increments. Spectra are calculated on June 18, 2018, 10:00–10:30 UTC.

quantifying wind plant blockage over simple terrain in an experimental setting. We employ an offline virtual scanning lidar to sample the velocity field and evaluate the blockage effect that would be seen by such a lidar deployed in the field.

A. Offline virtual lidar in WRF-LES

We perform virtual experiments on the flow field upstream of the King Plains wind plant using an offline virtual lidar informed by LES. The virtual lidar samples the three-dimensional LES velocity field to estimate the line-of-sight (LoS) velocity at each distance. These virtual measurements can be used to reconstruct a particular flow feature, such as the induction zone[51] or wakes[52,53] of individual wind turbines. Virtual measurements also provide the opportunity to compare the complete three-dimensional, unsteady LES velocity field with that observed by a lidar and estimate errors and optimize sampling patterns to minimize uncertainties for field observations.[54–59]

Herein, we use the virtual lidar tool described in Robey and Lundquist,[59] modified to incorporate terrain. The radial velocity, u_r, is computed by interpolating the three-dimensional wind components to points along the beam and projecting onto the beam direction,

$$u_r = u \sin(\gamma) \cos(\alpha) + v \cos(\gamma) \cos(\alpha) + w \sin(\alpha), \quad (1)$$

where u, v, and w are the interpolated three-dimensional wind components from the LES, and γ and α are the azimuth and elevation angles

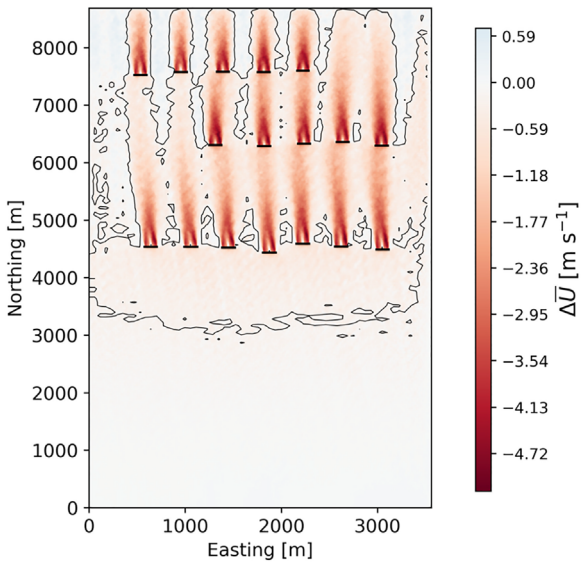

FIG. 8. Plan view of the hub-height, temporally averaged velocity deficit ($\Delta\bar{U} = \bar{U}_{GAD} - \bar{U}$). Turbines in the domain are represented as solid black lines. The black contour line represents a 2.5% velocity deficit.

for the lidar scan, respectively. The azimuth angle is measured clockwise from North. Moreover, the virtual lidar tool approximates the collection and internal processing of backscattered light by the application of a range-gate weighting function, ρ, (RWF). For this case, we simulate a pulsed scanning lidar with a full-width half-maximum parameter of 40 m. The LoS velocity, u_{LoS}, is given by the convolution of the projected wind velocities and the RWF,

$$u_{\mathrm{LoS}}(r) = \int_{-\infty}^{\infty} \rho(s) u_r(r+s)\, ds. \tag{2}$$

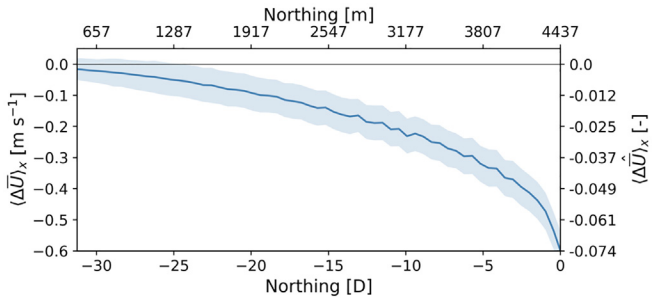

FIG. 9. Temporally and spatially averaged difference in velocity fields ($\langle\Delta\bar{U}\rangle_x = \langle\bar{U}_{GAD}\rangle_x - \langle\bar{U}\rangle_x$) for simulations with and without the GAD. The *x*-axis locates 0D at the southernmost turbine location ($y = 4437$ m in domain). The shaded area represents the 95% confidence intervals obtained from a bias-corrected and accelerated bootstrapping method. The secondary *y*-axis provides reference to the normalized velocity deficit ($\langle\Delta\bar{U}\rangle_x = \langle\Delta\bar{U}\rangle_x / \langle\bar{U}\rangle_x$). The secondary *x*-axis provides reference to the distance from the southern inflow boundary of the domain.

Finally, the horizontal velocity measured by the virtual lidar is calculated from the LoS velocity and corrected for the predominant wind direction, ϕ,

$$u_{scan} = \frac{u_{LoS}}{\cos(\gamma - \phi)\cos(\alpha)}. \tag{3}$$

The pulsed, Doppler scanning lidar simulated here is positioned on the nacelle of the southernmost turbine, providing measurements of the velocity field projected along the laser beam direction (LoS velocity) at hub height (Fig. 10). We use a plan-position indicator (PPI) scanning strategy at an elevation angle $\alpha = 0.1°$ from the horizon. The lidar scan covers azimuth angles, γ, between 150° and 210° at a scan rate of 2° s^{-1}. Range gates are defined between 126 m (1D) and 2400 m (19 D) with 50-m spatial resolution. The virtual lidar samples the three-dimensional velocity fields from the LES, output at 1 Hz for 10 min from 10:20 UTC to 10:30 UTC on June 18, 2018. Quasi-

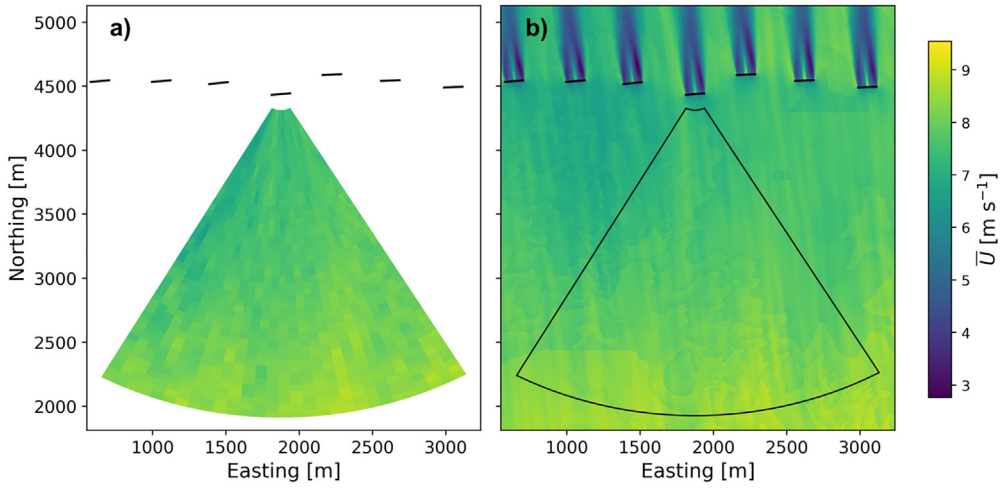

FIG. 10. Time-averaged velocity field from the virtual lidar (a) and the LES (b) at the same height above sea level ($z = 417$ m ASL). Virtual measurements represent the flow field as seen from a nacelle-mounted lidar on the center turbine in our domain. Wind turbines are represented by solid black lines.

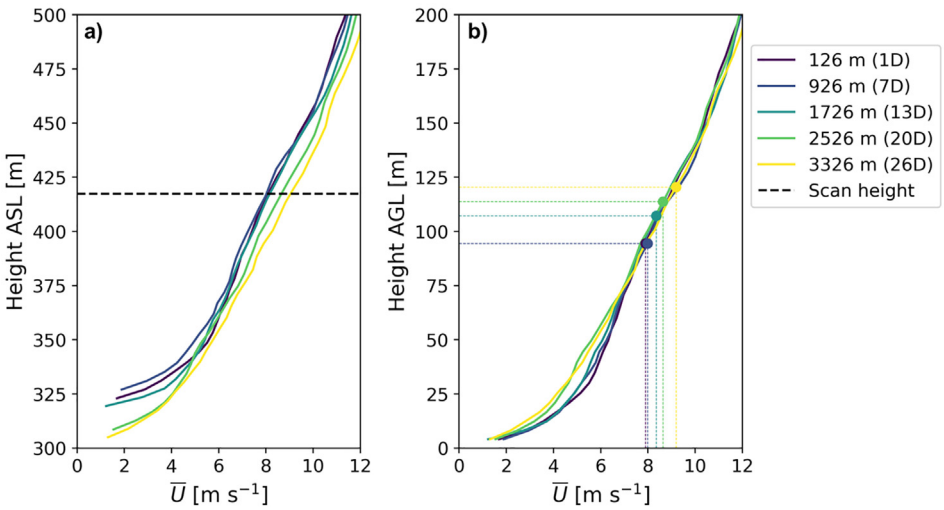

FIG. 11. Horizontal wind speed profiles color-coded for multiple distances upstream of the virtual lidar. Panel (a) illustrates the lidar scan height and the wind speed profile referenced with terrain. Panel (b) shows the wind speed profile referenced above the surface and the lidar scan height. The colored dots and dashed lines in (b) display the lidar scan height referenced above the surface at each location upstream of the lidar.

steady-state atmospheric conditions at this time facilitate the comparison between the lidar and LES.

B. Terrain effects

The velocity field measured by the lidar scan is influenced by changes in terrain elevation (Fig. 11). The virtual lidar samples the velocity field at a constant elevation above sea level (ASL) [Fig. 11(a)]. Thus, small changes in terrain elevation result in the lidar sampling the velocity field at different heights above the surface [Fig. 11(b)]. Small changes in terrain elevation displace the velocity profile upward or downward and, in an environment with large shear, these vertical displacements result in large fluctuations in the velocity sampled at a constant elevation above sea level. From now on, we refer to the local changes in horizontal wind speed at a constant height ASL resulting from local variations in terrain elevation as terrain effects (U_{terr}).

Terrain effects can overshadow wind plant blockage. Figure 12 demonstrates the variations in horizontal velocity as a result of sampling the velocity field at a constant elevation ASL over the region upstream of the wind plant. The changes in horizontal wind speed at a constant height ASL for the LES without the GAD (light-blue line in Fig. 12) primarily represent terrain effects (U_{terr}). Wind speed at $z = 417$ m ASL (i.e., 90 m AGL at the southernmost turbine location) changes from 8.35 to 7.61 m s^{-1} over 2457 m (from $y = -20$D to $y = -0.5$D) in the LES without the GAD. The variations in horizontal wind speed for the LES with the GAD (dark-blue in Fig. 12) represent the superposition of wind plant blockage and terrain effects. For the topography at this location and southerly flow, terrain effects (U_{terr}) denote sampling of the horizontal velocity profile at decreasingly lower heights above the surface from the river valley up to the wind plant location (see Fig. 13 for a schematic). While we found the induction zone is characterized by velocity deficits $\Delta U \sim 0.1$ m s^{-1} (see Sec. VI), terrain effects from the river valley produce spatial changes in wind speed close to 1 m s^{-1} over the same distance.

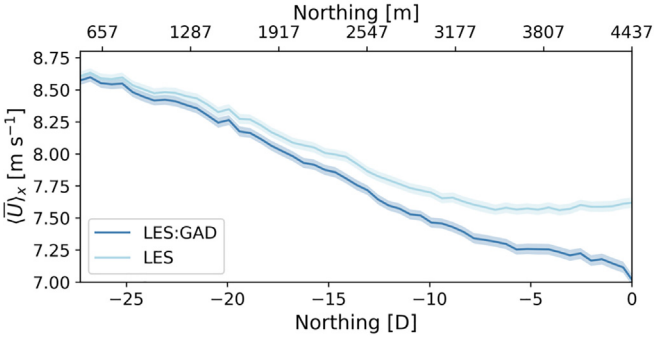

FIG. 12. Temporally and spatially averaged velocity field upstream of wind plant for simulations with and without the GAD at a constant height $z = 417$ m ASL. The color-coded shaded areas represent the 95% confidence intervals obtained from a bias-corrected and accelerated bootstrapping method. The x-axis locates 0D at the southernmost turbine location ($y = 4437$ m in domain). The secondary x-axis provides reference to the distance from the southern inflow boundary of the domain.

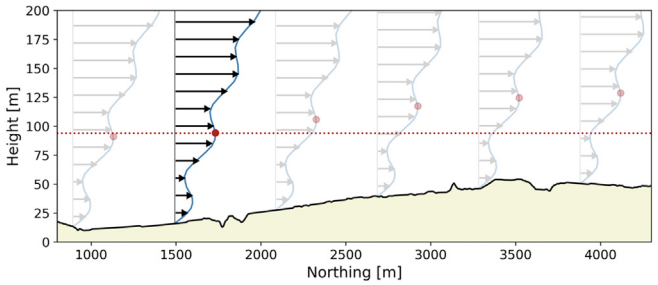

FIG. 13. Schematic exemplifying how changes in terrain elevation affect the velocity field measured by a scanning lidar at a constant height ASL. The lidar sampling height is denoted by the dotted red line. The schematic also exemplifies the procedure of translating the velocity profile over the entire domain. A single reference wind speed profile (full color) is translated over the entire domain (light color) to quantify terrain effects (U_{terr}). The red circles illustrate the lidar scan height at the location of the reference velocity profile (full color).

C. Differentiating between terrain effects and wind plant blockage using field-like observations

Both the virtual lidar velocity field and the LES velocity field qualitatively demonstrate a "slowdown" as the southerly flow approaches the turbine array. However, that slowdown also occurs in the simulation without the turbines. Note that the observed slowdown is not caused by curvature of the flow but rather by sampling the velocity field at different heights above the surface. Because that information (the velocity field without turbines) would not be available in a field experiment, the challenge is to distinguish the blockage effect from the other heterogeneity in the flow (i.e., terrain effects).

In simple terrain, the time-averaged velocity profile at one location provides a first-order approximation to the velocity profile nearby. A first-order Taylor expansion on the velocity profile gives $\bar{U}(\mathbf{x}, z) \approx \bar{U}(\mathbf{x}_0, z) + \frac{\partial \bar{U}}{\partial x_i}(x_i - x_{i0})$ for $i = 1, 2$. In idealized conditions (i.e., no changing weather patterns) and flat terrain, $\frac{\partial \bar{U}}{\partial x_i}$ is zero. Though our simulations are not idealized or in flat terrain, central Oklahoma is characterized by simple terrain ($\Delta z_{terr} \sim 10$ m for $\Delta x \sim 1000$ m) and June 18, 2018, is characterized by slowly varying weather at this location. Moreover, the averaged spatial variations in hub-height wind speed in our LES domain are very small ($\langle \frac{\partial \bar{U}}{\partial x} \rangle_{xy} \sim 10^{-6}\, s^{-1}$, $\langle \frac{\partial \bar{U}}{\partial y} \rangle_{xy} \sim 10^{-5}\, s^{-1}$), suggesting that $\bar{U}(\mathbf{x}, z) \approx \bar{U}(\mathbf{x}_0, z)$ gives small errors ($\sim$0.1 m s^{-1}) when $|\mathbf{x} - \mathbf{x}_0| < 10$ km.

We can estimate the terrain effects (U_{terr}) measured by the lidar by translating a single velocity profile over the entire domain. Figure 13 provides a schematic exemplifying this procedure. A velocity profile, time-averaged to exclude turbulence fluctuations, is sampled at a reference location far upstream of the wind plant (full colored profile in Fig. 13), so it is minimally affected by blockage. Terrain effects are estimated by translating the reference velocity profile over the entire domain (light colored profiles in Fig. 13) and sampling the resulting velocity field at a constant elevation above sea level (red dotted line in Fig. 13). Note that the reference velocity profile is sampled from the LES with the GAD, as would be done via tower or lidar in a field experiment.

Sampling the reference velocity profile at different locations upstream of the wind plant provides different approximations of the terrain effects (Fig. 14). Nonetheless, the translated velocity field from every location [gray lines in Fig. 14(a)] captures the decreasing trend in the horizontal wind speed due to terrain effects [black line in Fig. 14(a)]. We find the optimal location of the reference velocity profile by comparing the translated velocity field (gray lines in Fig. 14) with the velocity field from the LES without the GAD (black line in Fig. 14) over the region upstream of the wind plant. In this way, the translated velocity field should only represent terrain effects. Translating the velocity profile from a reference location $(x, y) = (2650, 1250$ m) minimizes the root mean square error (0.0028 m^2 s^{-2}) and gives a high correspondence ($R^2 = 0.975$) between the translated velocity field and terrain effects.

Translating a single wind speed profile enables the removal of terrain effects from the lidar scan to reveal the induction zone of the wind plant (Fig. 15). The spatially and temporally averaged terrain effects velocity field closely matches the velocity field from the WRF-LES without the turbines [Fig. 15(a)]. Note that the lidar and LES-GAD display small differences between 1.3D and 7D upstream of the wind plant [Fig. 15(a)] because of different spatial-averaging regions. Data from the virtual lidar are averaged over the scan area [see Fig. 10(a)], whereas the LES-GAD is averaged over the region upstream of the wind plant. As a result, the spatial average from the LES-GAD is more impacted by blockage from the neighboring turbines in the first row of the wind plant, especially those closest to the west-most edge of the domain. The velocity deficit estimated from the

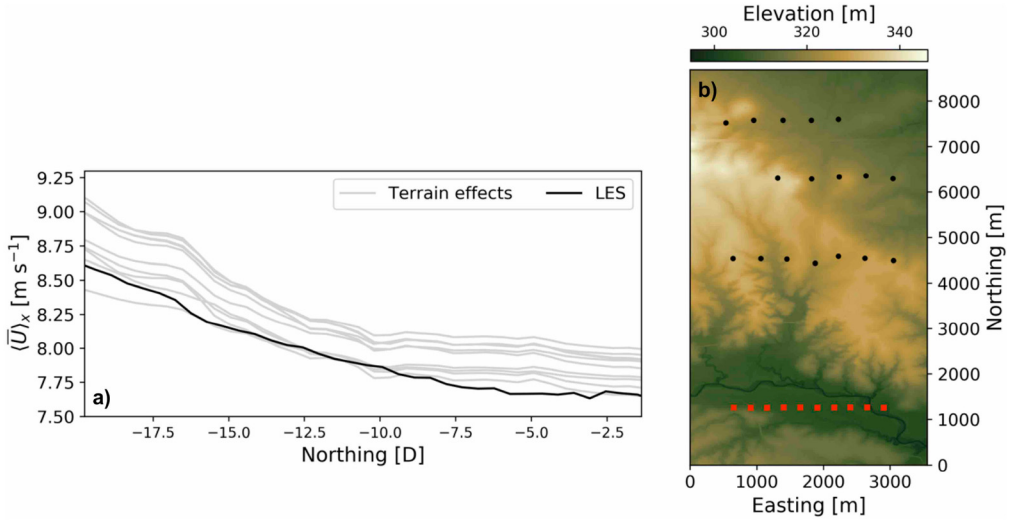

FIG. 14. Temporally and spatially averaged velocity field upstream of the wind plant at $z = 417$ m ASL (a). The gray lines represent terrain effects estimated using reference profiles at ten different locations in the domain. The topographic map (b) shows the relative location of the turbines (black circles) and locations for the reference wind speed profiles (red squares). The reference profiles are at the same latitude (36.336 117°, $y = 1260$ m in domain) and spaced longitudinally every 250 m from $x = 650$ to $x = 2900$ m in the domain. The velocity field in (a) is spatially averaged over the region upstream of the wind plant (from $x = 535$ to $x = 3050$ m). The x-axis in (a) locates 0D at the southernmost turbine location ($y = 4437$ m in domain).

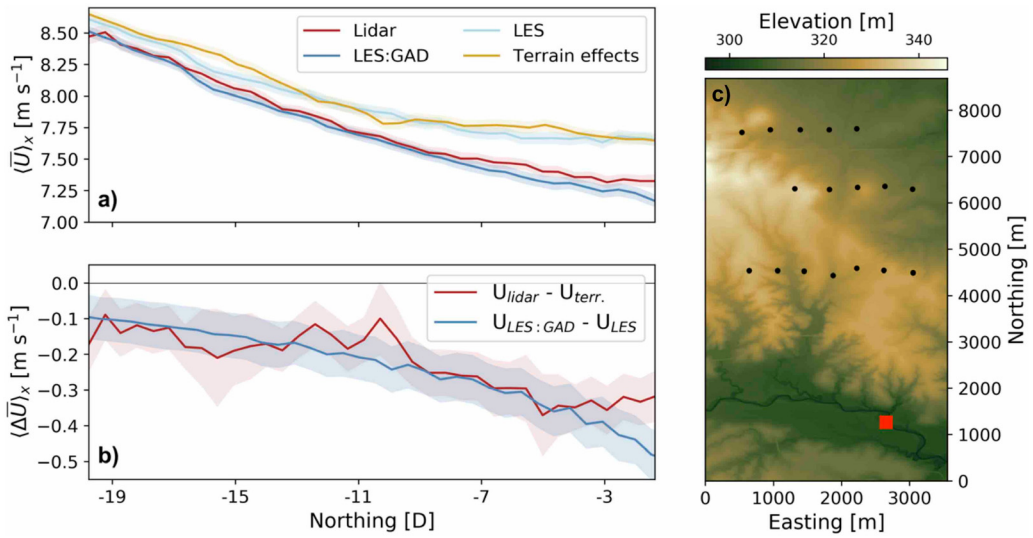

FIG. 15. Temporally and spatially averaged velocity field (a) and velocity deficit (b) upstream of the wind plant. The topographic map (c) shows the relative location of the turbines (black circles) and the reference location for the wind speed profile (red square) used to estimate terrain effects. The velocity field is spatially averaged over the region upstream of the wind plant (from $x = 535$ to $x = 3050$ m) for the LES:GAD, LES, and terrain effects. For the lidar, the velocity field is spatially averaged over the scan area [see Fig. 10(a)]. The x-axis in (a) and (b) locates 0D at the southernmost turbine location ($y = 4437$ m in domain). The color-coded, shaded areas in (a) and (b) represent the 95% confidence intervals for each case obtained from a bias-corrected and accelerated bootstrapping method.

lidar scan displays the same trend as the velocity deficit from the LES-GAD simulations ($R^2 = 0.87$) [Fig. 15(b)]. The root mean square error between the velocity deficit from the LES and the velocity deficit estimated from the lidar scan is 0.003 m s^{-1}. However, the magnitude of velocity deficit still displays considerable errors at multiple locations upstream of the wind plant derived from the assumptions made in estimating the terrain effects.

An inadequate selection of the location of the reference wind speed profile can result in significant errors when differentiating between the induction zone of a wind plant and terrain effects. Figure 16 exemplifies how translating the velocity profile from tendifferent

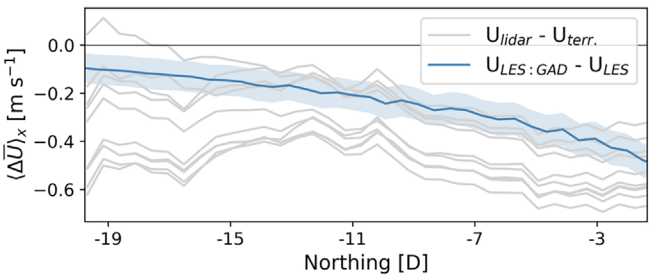

FIG. 16. Temporally and spatially averaged velocity deficit upstream of the wind plant. The gray lines represent different approximations of the induction zone, where terrain effects are estimated using reference profiles at the ten different locations in the domain shown in Fig. 14(b). The velocity field is spatially averaged over the region upstream of the wind plant (from $x = 535$ m to $x = 3050$ m) for the LES:GAD, LES, and terrain effects. For the lidar, the velocity field is spatially averaged over the scan area [see Fig. 10(a)]. The x-axis in locates 0D at the southernmost turbine location ($y = 4437$ m in domain). The color-coded, shaded area represents the 95% confidence interval obtained from a bias-corrected and accelerated bootstrapping method.

locations can result in large errors when estimating the induction zone of the wind plant. Even though the translated velocity field from every location captures the decreasing trend in the horizontal wind speed upstream of the wind plant (i.e., terrain effects), the spread in the blockage estimates ($U_{\text{lidar}} - U_{\text{terr}}$) is of the same order of magnitude as the blockage effect we are trying to measure. For instance, calculating terrain effects using a reference profile at $(x, y) = (2150, 1260$ m) gives a blockage estimate of -0.51 m s^{-1} 16D upstream of the wind plant, whereas calculating terrain effects using a reference profile at $(x, y) = (648, 1260$ m) gives a blockage estimate of -0.05 m s^{-1} at the same location.

VIII. DISCUSSION AND CONCLUSIONS

Wind plant blockage reduces turbine power production in wind plants. As a result, energy production for operational wind plants can be lower than expected.[3,10] However, the magnitude of the velocity slowdown and the physical mechanisms amplifying wind plant blockage are not yet well understood. A limited set of field experiments have provided some insight into the blockage effect upstream of wind turbine arrays. Most studies agree that the velocity slowdown in the induction zone is two orders of magnitude smaller than the freestream velocity ($\sim 0.01 U_\infty$),[3,12–14,18] making it very difficult to quantify experimentally. To overcome this difficulty, we perform WRF-LES of the King Plains wind plant in central Oklahoma to characterize the blockage effect. We also propose a methodology for experimentally quantifying wind plant blockage in regions with simple terrain and evaluate the uncertainties associated with this procedure.

Velocity reductions in the induction zone upstream of a subsection of the King Plains wind plant remain in the single-digit percentage range (Fig. 9). The velocity deficit 24D upstream of the first turbine row is 0.056 m s^{-1} (0.7%). Beyond 24D upstream in this case,

the velocity slowdowns are not statistically significant (95% confidence level). Bleeg *et al.*[3] and Schneemann *et al.*[12] also measured single-digit percentage slowdowns upstream of wind plants. For example, Bleeg *et al.*[3] calculated average wind speed deficits of 3.4% and 1.9% 2D and 7–10D upstream, respectively, for multiple wind plants surrounded by meteorological masts. In comparison, in these stably stratified conditions, we find velocity reductions of 5.4% and 3.19% 2D and 8D upstream, respectively. Similarly, Schneemann *et al.*[12] found wind speed is reduced by ∼4% over a distance of 25 rotor diameters (from 30D to 5D upstream of the wind plant), comparable to our results over the same distance ($\langle \Delta \tilde{U} \rangle_x = -3.9\%$ from 30D to 5D upstream of our wind plant).

Our findings disagree with some idealized studies. Wu and Porté-Agel[7] and Allaerts and Meyers[4] find observable wind speed decelerations extending 7 km upstream of the wind plant, with deficits close to 10% 10D upstream of the first turbine row. They attribute these large (∼10%) flow decelerations to gravity waves propagating upstream in their domains.[4,7] Wu and Porté-Agel[7] characterize the blocking behavior of the flow using the Froude number ($Fr = U/\sqrt{g' z_i}$), where U is the boundary-layer bulk velocity, g' is the reduced gravity, and z_i is the boundary layer height. They suggest gravity waves amplify the blockage effect in subcritical flow ($Fr < 1$), where pressure disturbances propagate upstream.[7] Atmospheric conditions in both stably stratified flows in the Allaerts and Meyers[4] simulations also favor upstream propagation of pressure disturbances ($Fr = 0.83, 0.9$). The Froude number in our simulations ($Fr = 1.27$) is characteristic of supercritical flow ($Fr > 1$); thus, pressure disturbances do not amplify wind plant blockage. Furthermore, both Wu and Porté-Agel[7] and Allaerts and Meyers[4] simulate larger wind plants (>120 turbines) that span the entire domain in the cross-stream direction; thus, the streamwise flow slowdown is entirely transformed into vertical motions, likely promoting gravity wave initiation. Additionally, Bleeg and Montavon[17] and Strickland and Stevens[33] found sensitivity of blockage to the relative size of the domain and wind plant, which is different between our simulations.

Upcoming field experiments can provide some quantitative estimates with uncertainties of the blockage effect and its extent. However, the small velocity deficit that characterizes the induction zone can be difficult to measure experimentally, especially in onshore environments with other flow heterogeneities. Blockage has only been quantified on shore using long-term observations before and after COD.[3,13] However, having long-term wind speed measurements before and after COD is impractical, forcing future field campaigns to quantify blockage employing a scanning-lidar-based methodology such as that used by Schneemann *et al.*[12] Upcoming field experiments in operational onshore wind plants, such as AWAKEN,[24] can further our understanding of the blockage effect. We perform virtual measurements of the induction zone of the King Plains wind plant using an offline virtual scanning lidar applied to our LES. By comparing the fully resolved LES velocity fields with the horizontal velocity computed by the virtual lidar, we evaluate the difficulties in measuring blockage in simple terrain.

Although the terrain variations in the AWAKEN domain are subtle, these local changes in terrain elevation displace the velocity profile vertically, adding variability to the horizontal velocity sampled at a constant height ASL and enhancing the difficulty of measuring the velocity slowdown upstream of a wind plant. We refer to this variability as terrain effects. A scanning lidar in PPI mode aligned with the horizon samples the velocity field at a constant elevation above sea level; however, if terrain elevation changes over the scan area, the lidar samples the velocity field at different heights above the ground (Fig. 11). Topography upstream of the King Plains wind plant is characterized by a river valley (∼22D upstream) and sloping terrain (∼1% slope), with a maximum elevation change of 37 m (Fig. 2). Sampling the LES velocity field at a constant height above sea level, like a scanning lidar, results in large variability in the horizontal wind speed upstream of the wind plant (Fig. 12). It is widely known that changes in the curvature of the flow caused by terrain add a bias in profiling lidar measurements.[54,55,60–64] However, to our knowledge, the effect of changes in terrain elevation has not been explicitly studied for scanning lidars.

Wind speed variability caused by terrain is of the same magnitude as the slowdowns caused by wind plant blockage (Fig. 15). Terrain effects, as measured by a scanning lidar, account for a ∼0.8 m s^{-1} change in wind speed upstream of the wind plant given that the velocity profile is gradually sampled at lower heights above the surface from the river valley up to the first turbine row (Fig. 11). The variability in horizontal wind speed caused by changes in topography is larger than the precision of state-of-the-art scanning lidars (the precision of the Halo Photonics Streamline lidar is <0.2 m s^{-1} for SNR > −17 dB[65]) and the largest deceleration caused by blockage (∼0.6 m s^{-1}).

Field observations require a procedure to differentiate blockage from terrain effects. We propose a methodology to isolate terrain effects from blockage that is based on translating a single velocity profile, sampled far away from the wind plant, over the region upstream of the turbines (see Fig. 13 for a schematic). By sampling the translated velocity field at a constant height ASL, we quantify the local changes in wind speed caused by local changes in topography and differentiate them from blockage (Fig. 15). However, the estimate of terrain effects is sensitive to the selection of the reference location for the velocity profile. Furthermore, our methodology does not account for other spatial heterogeneities, such as accelerations due to the curvature of the terrain or variations in land cover characteristics. Curvature of the terrain can produce local accelerations of the winds close to the surface, as shown by profiling lidars in complex terrain.[54,55,60–64] Additionally, our analysis is for atmospheric conditions that change very slowly in time, favoring the application of our proposed methodology. Applying our approach for another time with more transient conditions might be challenging.

An improper selection of the reference location for estimating terrain effects can result in the under- or overestimation of the blockage effect. Figures 14 and 16 exemplify the variability in the estimated terrain effects from ten different reference locations within 2.25 km of one another and the corresponding errors in the induction zone estimated from the virtual measurements, respectively. This large variability highlights the importance of coupling simulation and experimental studies for appropriately quantifying terrain effects.

Wind direction is also expected to modify terrain effects. In this location, lidar scans from easterly winds are expected to capture smaller changes in horizontal wind speed due to local topography given that the river valley runs approximately from east to west and the local changes in terrain to the east are small. Expanding this methodology to other locations will require careful consideration of the topographic variability.

We emphasize that the results presented here are for a specific atmospheric condition (i.e., atmospheric stability, wind direction, wind speed, shear, etc.) and only for a subsection of a specific wind plant. Blockage from the 88 turbines in the King Plains wind plant could likely be larger than found here. Also, the methodology for differentiating between blockage and terrain effects is highly sensitive to the reference location of the velocity profile. We hypothesize the optimal location for estimating terrain effects changes with wind direction, given that the fetch changes. Future studies of blockage at the King Plains wind plant could include validation of the magnitude of the deceleration and spatial extent of the induction zone. The results presented here also suggest that future experimental studies quantifying blockage on shore using scanning lidars should attempt to estimate terrain effects and differentiate them from the induction zone of the wind plant. Another area of future research relates to the uncertainties associated of measuring blockage under considerable wind loading. Under extreme wind loading, the fore-aft displacement of the nacelle can be on the order of 1 m,[66,67] changing the elevation angle of the scan by approximately 0.2°. Over the long distances associated with blockage ($\sim 10^3$ m), a 0.2° change in elevation angle results in sampling the velocity profile 13 m higher than at the turbine location, adding uncertainty to the measurements.

ACKNOWLEDGMENTS

We would like to acknowledge supportive discussions with the AWAKEN simulation group led by Dr. Nicholas Hamilton. This work was supported by an agreement with NREL under APUP UGA-0-41026-125. This work was authored in part by the National Renewable Energy Laboratory, operated by Alliance for Sustainable Energy, LLC, for the U.S. Department of Energy (DOE) under Contract No. DE-AC36-08GO28308. Funding provided by the U.S. Department of Energy Office of Energy Efficiency and Renewable Energy Wind Energy Technologies Office. The views expressed in the article do not necessarily represent the views of the DOE or the U.S. Government. The U.S. Government retains and the publisher, by accepting the article for publication, acknowledges that the U.S. Government retains a nonexclusive, paid-up, irrevocable, worldwide license to publish or reproduce the published form of this work, or allow others to do so, for U.S. Government purposes. J.D.M. and R.S.A. contributed under the auspices of the U.S. Department of Energy (DOE) by Lawrence Livermore National Laboratory, under Contract No. DE-AC52-07NA27344.

AUTHOR DECLARATIONS

Conflict of Interest

The authors have no conflicts to disclose.

Author Contributions

Miguel Sanchez Gomez: Conceptualization (equal); Data curation (lead); Formal analysis (lead); Methodology (equal); Visualization (lead); Writing – original draft (lead); Writing – review & editing (equal). **Julie Lundquist:** Conceptualization (equal); Formal analysis (supporting); Methodology (equal); Supervision (lead); Writing – review & editing (equal). **Jeff Mirocha:** Formal analysis (supporting); Software (lead); Writing – review & editing (equal). **Robert Arthur:** Formal analysis (supporting); Software (lead); Writing – review & editing (equal). **Domingo Munoz-Esparza:** Formal analysis (supporting); Software (lead); Writing – review & editing (supporting). **Rachel Robey:** Software (equal); Writing – review & editing (equal).

DATA AVAILABILITY

The data that support the findings of this study are available from the corresponding author upon reasonable request.

APPENDIX: SENSITIVITY TO GRID RESOLUTION

A grid sensitivity analysis is performed to determine the dependence of resolved turbulence on the grid cell size. To this end, we fix the physical size of the innermost domain (D04) to $(L_x, L_y, L_z) = (3, 9, \text{and } 16\,\text{km})$ and vary the horizontal and vertical resolution. We evaluate the spatial and temporal evolution of turbulence resolved by different grid configurations over a 40 min time period. Spin-up time for domains D01, D02, and D03 is the same as described in Sec. IV.

Turbulence propagates over the entire domain 10 min after initialization in every domain configuration (Fig. 17). Every simulation displays an initial overshoot in turbulence kinetic energy (TKE), a result of turbulence structures forming and propagating downstream of the southern inflow boundary.

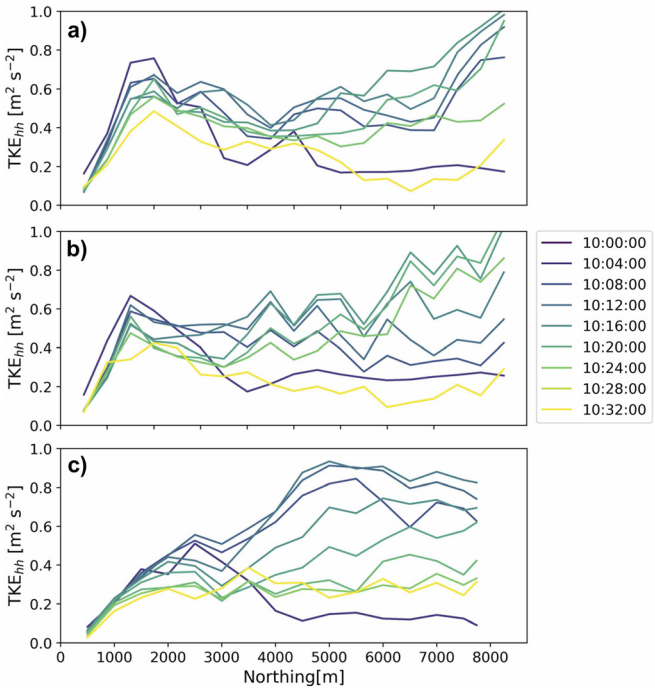

FIG. 17. Streamwise development of hub-height turbulence kinetic energy ($\bar{k}_{hh}$) for (a) $\Delta x = 12.5$ and $\Delta z_s = 8$ m, (b) $\Delta x = 8$ and $\Delta z_s = 8$ m, and (c) $\Delta x = 3.9$ and $\Delta z_s = 4$ m. Colored lines indicate the temporal evolution of TKE on June 18, 2018. Data at the inflow and outflow domain boundaries are excluded. Turbulence is estimated using a 10 min moving variance.

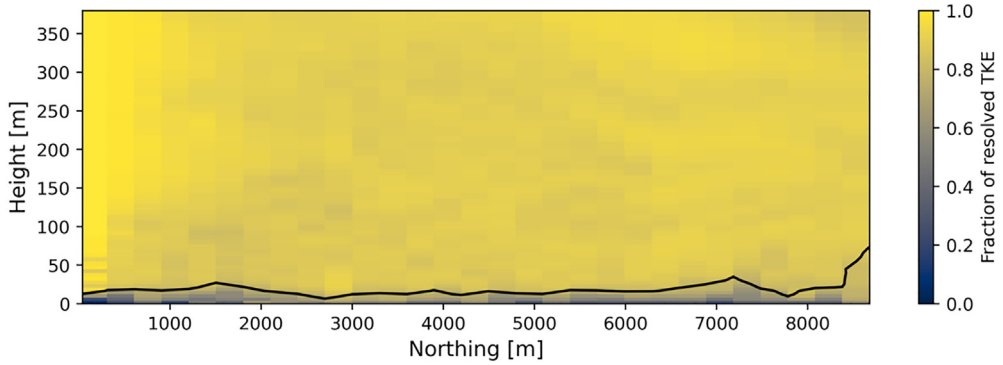

FIG. 18. Fraction of resolved TKE in the surface layer. The solid, black line shows the height at which 80% of TKE is resolved at each streamwise location. Turbulence statistics are estimated after 30 min of spin-up.

Turbulence only reaches a steady and stationary state with the highest grid resolution [Fig. 17(c)]. After 30 min of simulation time, TKE is highly non-stationary for $\Delta x = 12.5$ and $\Delta x = 8$ m [Figs. 17(a) and 17(b)]. For the coarser-resolution simulations, turbulence generated from the cell-perturbation method at the inflow boundary decays spatially. Conversely, turbulence displays small spatial and temporal variations for $\Delta x = 3.9$ m [Fig. 17(c)] after 30 min and 1 km away from the inflow boundary.

In addition of evaluating the spatial and temporal evolution of turbulence, we consider the fraction of resolved TKE in the surface layer. For the nonlinear backscatter and anisotropy subgrid-scale turbulence model,[31] the total turbulence kinetic energy ($\bar{k}_t$) is given by $\bar{k}_t = \frac{1}{2}(\overline{u_i' u_i'} + m_{ii}) + k_{SGS}$, where $\overline{u_i' u_i'}$ represents the resolved TKE, m_{ii} are the normal subgrid-scale stress components, and k_{SGS} is the subgrid-scale turbulence kinetic energy. At least 80% of the total TKE is resolved above 35 m in the higher-resolution simulation (Fig. 18). For large-Eddy simulations with near-wall resolution, Pope[68] suggests 80% of the energy be resolved. For evaluating wind plant blockage, we are interested in resolving turbulence within the turbine rotor layer. Figure 18 shows turbulence is properly represented in the surface layer over the entire domain.

REFERENCES

[1]R. B. Smith, "Gravity wave effects on wind farm efficiency," Wind Energy **13**, 449–458 (2009).
[2]R. Ebenhoch, B. Muro, J-k Dahlberg, P. Berkesten Hägglund, and A. Segalini, "A linearized numerical model of wind-farm flows: A linearized numerical model of wind-farm flows," Wind Energy **20**, 859–875 (2017).
[3]J. Bleeg, M. Purcell, R. Ruisi, and E. Traiger, "Wind farm blockage and the consequences of neglecting its impact on energy production," Energies **11**, 1609 (2018).
[4]D. Allaerts and J. Meyers, "Gravity waves and wind-farm efficiency in neutral and stable conditions," Boundary-Layer Meteorol. **166**, 269–299 (2018).
[5]D. Allaerts and J. Meyers, "Boundary-layer development and gravity waves in conventionally neutral wind farms," J. Fluid Mech. **814**, 95–130 (2017).
[6]D. Allaerts and J. Meyers, "Sensitivity and feedback of wind-farm-induced gravity waves," J. Fluid Mech. **862**, 990–1028 (2019).
[7]K. Wu and F. Porté-Agel, "Flow adjustment inside and around large finite-size wind farms," Energies **10**, 2164 (2017).
[8]X. Wang, P. Guo, and X. Huang, "A review of wind power forecasting models," Energy Procedia **12**, 770–778 (2011).
[9]M. Brower, *Wind Resource Assessment: A Practical Guide to Developing a Wind Project*, edited by M. Brower (Wiley, 2012).
[10]Ørsted, "Company announcement no. 28/2019: Ørsted presents update on its long-term financial targets," Announcement No. 28/2019 (Ørsted, 2019); available at: https://orsted.com/ja/company-announcement-list/2019/10/1937002.
[11]J. C. Y. Lee and J. K. Lundquist, "Observing and simulating wind-turbine wakes during the evening transition," Boundary-Layer Meteorol. **164**, 449–474 (2017).
[12]J. Schneemann, F. Theuer, A. Rott, M. Dörenkämper, and M. Kühn, "Offshore wind farm global blockage measured with scanning lidar," Wind Energy Sci. **6**, 521–538 (2021).
[13]C. Jacquet, D. Apgar, V. Chauchan, R. Storey, S. Kern, and S. Davoust, "Farm blockage model validation using pre and post construction LiDAR measurements," J. Phys.: Conf. Ser. **2265**, 022009 (2022).
[14]A. Sebastiani, F. Castellani, G. Crasto, and A. Segalini, "Data analysis and simulation of the lillgrund wind farm," Wind Energy **24**, 634–648 (2021).
[15]A. Segalini, "Linearized simulation of flow over wind farms and complex terrains," Philos. Trans. R. Soc. A **375**, 20160099 (2017).
[16]E. Branlard and A. R. Meyer Forsting, "Assessing the blockage effect of wind turbines and wind farms using an analytical vortex model," Wind Energy **23**, 2068–2086 (2020).
[17]J. Bleeg and C. Montavon, "Blockage effects in a single row of wind turbines," J. Phys.: Conf. Ser. **2265**, 022001 (2022).
[18]A. Segalini and J. Dahlberg, "Blockage effects in wind farms," Wind Energy **23**, 120–128 (2020).
[19]E. Bou-Zeid, C. Meneveau, and M. B. Parlange, "Large-eddy simulation of neutral atmospheric boundary layer flow over heterogeneous surfaces: Blending height and effective surface roughness," Water Resour. Res. **40**, W02505, https://doi.org/10.1029/2003WR002475 (2004).
[20]D. V. Mironov and P. P. Sullivan, "Second-moment budgets and mixing intensity in the stably stratified atmospheric boundary layer over thermally heterogeneous surfaces," J. Atmos. Sci. **73**, 449–464 (2016).
[21]*Mountain Weather Research and Forecasting: Recent Progress and Current Challenges*, Springer Atmospheric Sciences, edited by B. J. Snyder, Fotini K. Chow, and Stephan F. J. De Wekker (Springer, 2013).
[22]B. Zhou and F. K. Chow, "Nested large-eddy simulations of the intermittently turbulent stable atmospheric boundary layer over real terrain," J. Atmos. Sci. **71**, 1021–1039 (2014).
[23]B. Vanderwende and J. K. Lundquist, "Could crop height affect the wind resource at agriculturally productive wind farm sites?," Boundary-Layer Meteorol. **158**, 409–428 (2016).
[24]P. Moriarty, N. Hamilton, M. Debnath, H. Tommy, B. Isom, J. K. Lundquist, D. Maniaci, B. Naughton, R. Pauly, J. Roadman, W. Shaw, J. van Dam, and S. Wharton, "American WAKE experimeNt (AWAKEN)," Report No. NREL/TP-5000-75789 (National Renewable Energy Laboratory, Golden, CO, USA, 2020).
[25]R. Krishnamurthy, R. K. Newsom, D. Chand, and W. J. Shaw, "Boundary layer climatology at ARM southern great plains," Report No. PNNL-30832 (Pacific Northwest National Laboratory, Richland, WA, USA, 2021).

[26]M. Debnath, P. Moriarty, R. Krishnamurthy, E. Q. Nicola Bodini, and S. Letizia, "Characterization of wind speed and directional shear at the awaken field campaign site" (submitted, 2022).
[27]T. Shippert, R. Newsom, and L. Riihimaki, "Doppler lidar horizontal wind profiles (dlprofwind4news)," Atmospheric Radiation Measurement (ARM), (ARM User Facility, 2022), (last accessed 05-22-2022) (2016).
[28]N. Bodini, J. K. Lundquist, and P. Moriarty, "Wind plants can impact long-term local atmospheric conditions," Sci. Rep. **11**, 22939 (2021).
[29]W. C. Skamarock, J. B. Klemp, J. Dudhia, D. O. Gill, Z. Liu, J. Berner, W. Wang, J. G. Powers, M. G. Duda, D. M. Barker, and X.-Y. Huang, "A description of the advanced research WRF model version 4" (National Center for Atmospheric Research, Boulder, CO, USA, 2019).
[30]Z. I. Janić, "The surface layer parameterization in the NCEP eta model," in *11th Conference on Numerical Weather Prediction* (American Meteorology Society, 1996), pp. 354–355.
[31]B. Kosović, "Subgrid-scale modelling for the large-eddy simulation of high-Reynolds-number boundary layers," J. Fluid Mech. **336**, 151–182 (1997).
[32]J. D. Mirocha, J. K. Lundquist, and B. Kosović, "Implementation of a nonlinear subfilter turbulence stress model for large-eddy simulation in the advanced research WRF model," Mon. Weather Rev. **138**, 4212–4228 (2010).
[33]J. M. Strickland and R. J. Stevens, "Investigating wind farm blockage in a neutral boundary layer using large-eddy simulations," Eur. J. Mech.-B/Fluids **95**, 303–314 (2022).
[34]M. H. Daniels, K. A. Lundquist, J. D. Mirocha, D. J. Wiersema, and F. K. Chow, "A new vertical grid nesting capability in the weather research and forecasting (WRF) model," Mon. Weather Rev. **144**, 3725–3747 (2016).
[35]U.S. Geological Survey. "1/3rd arc-second digital elevation models" (U.S. Geological Survey, Reston, VA, USA, 2020).
[36]J. Dewitz. "National land cover database 2019 products" (U.S. Geological Survey, Reston, VA, USA, 2021).
[37]S.-Y. Hong, J. Dudhia, and S.-H. Chen, "A revised approach to ice microphysical processes for the bulk parameterization of clouds and precipitation," Mon. Weather Rev. **132**, 103–120 (2004).
[38]E. J. Mlawer, S. J. Taubman, P. D. Brown, M. J. Iacono, and S. A. Clough, "Radiative transfer for inhomogeneous atmospheres: RRTM, a validated correlated-k model for the longwave," J. Geophys. Res. **102**, 16663–16682, https://doi.org/10.1029/97JD00237 (1997).
[39]J. Dudhia, "Numerical study of convection observed during the winter monsoon experiment using a mesoscale two-dimensional model," J. Atmos. Sci. **46**, 3077–3107 (1989).
[40]Z. I. Janić, "Nonsingular implementation of the Mellor Yamada level 2.5 scheme in the NCEP meso model," (2001).
[41]M. B. Ek, K. E. Mitchell, Y. Lin, E. Rogers, P. Grunmann, V. Koren, G. Gayno, and J. D. Tarpley, "Implementation of Noah land surface model advances in the National Centers for Environmental Prediction operational mesoscale Eta model," J. Geophys. Res. **108**, 8851, https://doi.org/10.1029/2002JD003296 (2003).
[42]Dataset: National Centers for Environmental Prediction (2015). "NCEP North American Mesoscale (NAM) 12 km analysis," Research Data Archive at the National Center for Atmospheric Research, Computational and Information Systems Laboratory.
[43]J. D. Mirocha, B. Kosovic, M. L. Aitken, and J. K. Lundquist, "Implementation of a generalized actuator disk wind turbine model into the weather research and forecasting model for large-eddy simulation applications," J. Renewable Sustainable Energy **6**, 013104 (2014).
[44]M. L. Aitken, B. Kosović, J. D. Mirocha, and J. K. Lundquist, "Large eddy simulation of wind turbine wake dynamics in the stable boundary layer using the weather research and forecasting model," J. Renewable Sustainable Energy **6**, 033137 (2014).
[45]R. S. Arthur, J. D. Mirocha, N. Marjanovic, B. D. Hirth, J. L. Schroeder, S. Wharton, and F. K. Chow, "Multi-scale simulation of wind farm performance during a frontal passage," Atmosphere **11**, 245 (2020).
[46]T. Shippert, R. Newsom, and L. Riihimaki, "Doppler lidar wind statistics profiles (dlprofwstats4news)," Atmospheric Radiation Measurement (ARM), (ARM User Facility, 2010), (last accessed 05-22-2022).
[47]S. Biraud, D. Billesbach, and S. Chan, "Carbon dioxide flux measurement systems (CO_2FLX60m)," Atmospheric Radiation Measurement (ARM), (ARM User Facility, 2022), (last accessed 05-22-2022).
[48]D. Muñoz-Esparza, B. Kosović, J. Mirocha, and J. van Beeck, "Bridging the transition from mesoscale to microscale turbulence in numerical weather prediction models," Boundary-Layer Meteorol. **153**, 409–440 (2014).
[49]D. Muñoz-Esparza, B. Kosović, J. van Beeck, and J. Mirocha, "A stochastic perturbation method to generate inflow turbulence in large-eddy simulation models: Application to neutrally stratified atmospheric boundary layers," Phys. Fluids **27**, 035102 (2015).
[50]B. Efron and R. J. Tibshirani, *An Introduction to the Bootstrap*, Monographs on statistics and Applied Probability (Chapman & Hall, 1993).
[51]A. R. Meyer Forsting, N. Troldborg, J. P. Murcia Leon, A. Sathe, N. Angelou, and A. Vignaroli, "Validation of a CFD model with a synchronized triple-lidar system in the wind turbine induction zone," Wind Energy **20**, 1481–1498 (2017).
[52]F. Fuertes and F. Porté-Agel, "Using a virtual lidar approach to assess the accuracy of the volumetric reconstruction of a wind turbine wake," Remote Sens. **10**, 721 (2018).
[53]M. van Dooren, D. Trabucchi, and M. Kühn, "A methodology for the reconstruction of 2D horizontal wind fields of wind turbine wakes based on dual-Doppler lidar measurements," Remote Sens. **8**, 809 (2016).
[54]S. Bradley, Y. Perrott, P. Behrens, and A. Oldroyd, "Corrections for wind-speed errors from sodar and lidar in complex terrain," Boundary-Layer Meteorol. **143**, 37–48 (2012).
[55]T. Rovers, "Correction of sodar wind speed bias in complex terrain situations," in EWEA, 2012.
[56]J. K. Lundquist, M. J. Churchfield, S. Lee, and A. Clifton, "Quantifying error of lidar and sodar Doppler beam swinging measurements of wind turbine wakes using computational fluid dynamics," Atmos. Meas. Tech. **8**, 907–920 (2015).
[57]C. Rahlves, F. Beyrich, and S. Raasch, "Scan strategies for wind profiling with Doppler lidar—An LES-based evaluation," Atmos. Meas. Tech. **15**, 2839–2856 (2021).
[58]P. Gasch, A. Wieser, J. K. Lundquist, and N. Kalthoff, "An LES-based airborne Doppler lidar simulator and its application to wind profiling in inhomogeneous flow conditions," Atmos. Meas. Tech. **13**, 1609–1631 (2020).
[59]R. Robey and J. K. Lundquist, "Behavior and mechanisms of Doppler wind lidar error in varying stability regimes," Atmos. Meas. Tech. **15**, 4585–4622 (2022).
[60]F. Bingöl, J. Mann, and D. Foussekis, "Conically scanning lidar error in complex terrain," Meteorol. Z. **18**, 189–195 (2009).
[61]S. Bradley, "A simple model for correcting sodar and lidar errors in complex terrain," J. Atmos. Oceanic Technol. **29**, 1717–1722 (2012).
[62]S. Bradley, A. Strehz, and S. Emeis, "Remote sensing winds in complex terrain—A review," Meteorol. Z. **24**, 547–555 (2015).
[63]T. Klaas, L. Pauscher, and D. Callies, "LiDAR-mast deviations in complex terrain and their simulation using CFD," Meteorol. Z. **24**, 591–603 (2015).
[64]A. Clifton, P. Clive, J. Gottschall, D. Schlipf, E. Simley, L. Simmons, D. Stein, D. Trabucchi, N. Vasiljevic, and I. Würth, "IEA wind task 32: Wind lidar identifying and mitigating barriers to the adoption of wind lidar," Remote Sens. **10**, 406 (2018).
[65]See https://halo-photonics.com/lidar-systems/stream-line-series/ for HALO Photonics, "Technical specifications HALO photonics streamline series" (Last accessed 05-22-2022).
[66]C. Sun, "Mitigation of offshore wind turbine responses under wind and wave loading: Considering soil effects and damage: Mitigation of offshore wind turbine responses under wind and wave loading: Considering soil effects and damage," Struct. Control Health Monit. **25**, e2117 (2018).
[67]C. Sun, V. Jahangiri, and H. Sun, "Performance of a 3D pendulum tuned mass damper in offshore wind turbines under multiple hazards and system variations," Smart Struct. Syst. **24**, 53–65 (2019).
[68]S. B. Pope, *Turbulent Flows*, 1st ed. (Cambridge University Press, 2000).